Observation of topological gravity-capillary waves in a water wave crystal

Nicolas Laforge, Vincent Laude, Franck Chollet, Abdelkrim Khelif, Muamer Kadic*

Institut FEMTO-ST, CNRS UMR 6174, Université de Bourgogne Franche-Comté, Besançon, France

E-mail: `muamer.kadic@femto-st.fr`

Yuning Guo, Romain Fleury

Laboratory of Wave Engineering (LWE), Ecole Polytechnique Fédérale de Lausanne (EPFL), Switzerland

Abstract. The discovery of topological phases of matter, initially driven by theoretical advances in quantum condensed matter physics, has been recently extended to classical wave systems, reaching out to a wealth of novel potential applications in signal manipulation and energy concentration. Despite the fact that wave propagation in many realistic media (metals at optical frequencies, polymers at ultrasonic frequencies) is inherently dispersive, topological wave transport in photonic and phononic crystals has so far been limited to ideal situations and proof-of-concept experiments involving dispersionless media. Here, we report the first experimental demonstration of topological edge states in a classical water wave system supporting highly dispersive wave propagation, in the intermediate regime of gravity-capillary waves. We use a stochastic method to rigorously take into account the inherent dispersion and devise a water wave crystal insulator supporting valley-selective transport at topological domain walls. Our measurements, performed with a high-speed camera under stroboscopic illumination, unambiguously demonstrate the possibility of valley-locked transport of water waves.

1. Introduction

Topological insulators are bulk insulators whose bands are characterized by a quantized number known as a topological invariant [1, 2], which cannot change upon continuous transformations of the band structure. This topological property of the bands implies the presence of edge states at topological interfaces, which is protected by the topology of the surrounding bulk insulators [3, 4, 5, 6, 7, 8, 9, 10]. Originally discovered in condensed matter systems, including Quantum-Hall [11, 12, 13, 14, 15, 16, 17, 18, 19] and Quantum Spin-Hall insulators [20, 21, 22, 23], the concept of topological transport has recently been transposed to various fields of classical wave physics, including optics [24, 25, 26], acoustics [8, 27, 28, 29], microwaves [12, 30], and mechanics [31, 32, 33, 34, 9], where it represents a promising way to transport signals and concentrate energy in a robust, symmetry-protected way. While classical analogs of Chern insulators [35, 28], quantum spin-Hall systems [36], and valley-Hall insulators [37, 8, 38, 39, 40] have been previously studied and demonstrated, prior arts have focused mainly on idealistic situations in which the dispersion of the host materials have been neglected or avoided. This drastic assumption, however, holds only for a small subset of the available physical platforms in which exploiting topological physics could have large practical implications. It does not hold, for instance, for water wave systems, which generally support highly dispersive surface waves [41]. Yet, controlling the energy carried by ocean waves, and forcing it to concentrate at a location where it can be harvested, would be a fascinating application of topological physics, providing topological edge modes are compatible with the highly dispersive character of these systems.

In this article, we demonstrate experimentally the relevance of topological physics in a classical wave system with strong dispersion, namely gravity-capillary waves at a water-air interface interacting with a water wave crystal. We use a stochastic method to obtain the dispersion relation in the crystal, using Bloch's theorem, and we design topological edge states based on valley conservation. Our measurements, based on direct imaging using a high-speed camera under stroboscopic illumination (see Fig. 1), demonstrate unambiguously the possibility of topological transport in systems with very strong dispersion, extending the reach of topological physics to a wealth of new physical platforms.

2. Theoretical and Experimental description

Gravity-capillary water waves are surface waves resulting from the balance of the potential energy of gravity forces and surface tension with the kinetic energy of a water column. As a result of body (volume) and interface (surface) contributions, their velocity is isotropic but inherently strongly dispersive and dependent on the water depth. In order to describe the propagation of gravity-capillary waves in the regime of small water elevation (as compared to the water depth), we consider the linear velocity potential theory for water waves [42, 43, 44]. In the absence of external forces, the vertical

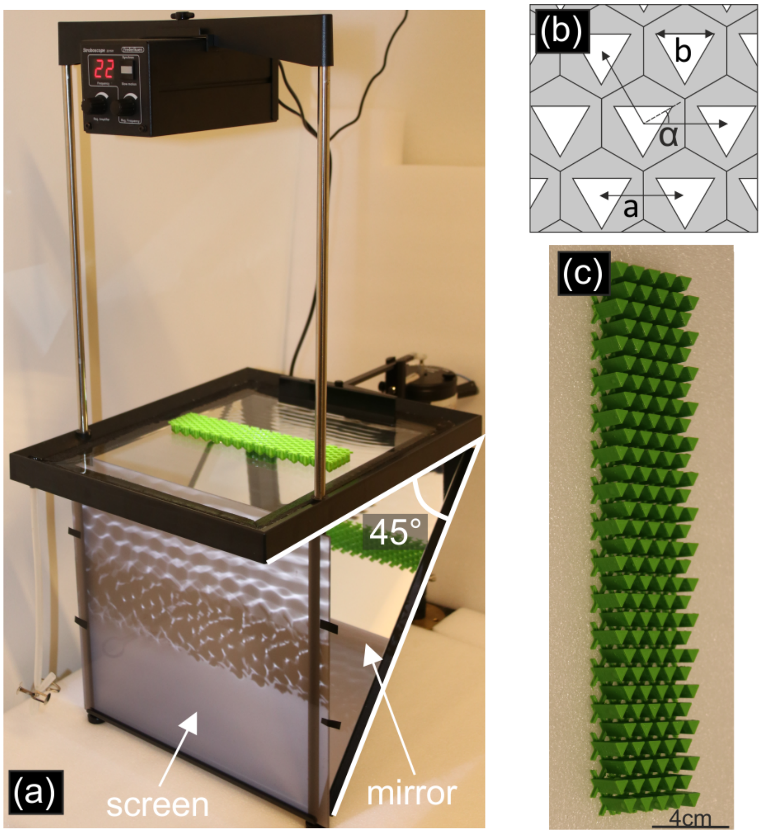

Figure 1. Experimental setup for observation of topological gravity-capillary waves in a water wave crystal. (a) The crystal sample (green color) is placed in a water tank. A mechanical straight paddle is exciting vertical motion of the water surface at the same frequency as the stroboscopic illumination. A mirror is placed at 45° below and reflects the image on a diffusive screen placed in front. (b) The hexagonal crystal is made of triangular pillars with $a = 8$ mm, $b = 6.4$ mm, and a variable orientation angle α (here $\alpha = 30°$). (c) A typical 3D-printed crystal sample made of PLA (polylactic acid) is shown.

displacement (elevation) of the liquid-air interface $\eta(x, y)$ satisfies the two-dimensional partial differential equation

$$\nabla \cdot (c_{\mathrm{p}} c_{\mathrm{g}} \nabla \eta) + \kappa^2 c_{\mathrm{p}} c_{\mathrm{g}} \eta = 0, \tag{1}$$

where c_{p} is the phase velocity, c_{g} is the group velocity, and κ is the wavenumber. A similar equation is satisfied by the horizontal part of the velocity potential [42]. We further recall that the dispersion relation between wavenumber and angular frequency ω for a horizontal liquid-air interface is given by

$$\omega^2 = g\kappa(1 + d_c^2\kappa^2)\tanh(\kappa h), \tag{2}$$

where g is the gravitational acceleration, h is the water depth, and d_c is the capillary length. The phase velocity is then

$$c_{\mathrm{p}} = \frac{\omega}{\kappa} = \sqrt{\frac{g}{\kappa}(1 + d_c^2\kappa^2)\tanh(\kappa h)} \tag{3}$$

and the group velocity is

$$c_{\mathrm{g}} = \frac{d\omega}{d\kappa} = \left(\frac{1}{2} + \frac{d_c^2\kappa^2}{1+d_c^2\kappa^2} + \frac{\kappa h}{\sinh(2\kappa h)}\right) c_{\mathrm{p}}, \tag{4}$$

where the capillary length is given by $d_c = \sqrt{\frac{\gamma}{g\rho}}$, with γ the surface tension and ρ the mass density of the liquid.

Inside the artificial crystal sample, Eq. (1) can be used to obtain Bloch waves and therefore band structures. Indeed, Eq. (1) can be recast as a Helmholtz equation for scalar waves in a dispersive medium

$$\nabla \cdot (A(\omega)\nabla\eta) + \omega^2 B(\omega)\eta = 0, \tag{5}$$

with coefficients $A(\omega) = c_{\mathrm{p}}c_{\mathrm{g}}$ and $B(\omega) = c_{\mathrm{g}}/c_{\mathrm{p}}$ depending explicitly on frequency. A Neumann boundary condition is considered at the interfaces between pillars and water, i.e. $\partial\eta/\partial n = 0$, where n is the normal to the interface [42, 43, 44]. Bloch waves have the form $\eta(x, y) = \eta_{\mathbf{k}}(x, y)\exp(\imath\mathbf{k}\cdot\mathbf{r})$, with $\mathbf{k}$ the Bloch wavevector and $\eta_{\mathbf{k}}$ the periodic part of the Bloch wave. Computing eigenvalues and eigenfunctions to obtain the Bloch waves of the crystal is not straightforward since the coefficients of the equation depend on frequency. We use instead the stochastic excitation method proposed by Laude and Korotyaeva [45]. The method considers all possible values of frequency ω and Bloch wavevector $\mathbf{k}$ and observes the response of the system to a spatially random force distributed inside the unit-cell. The finite element implementation for Eq. (5) follows the prescriptions in Ref. [45]. A further difficulty is that the model does not take into account certain interface effects between water and the solid pillars, including the formation of a meniscus as a result of capillary forces. As the distance between pillars is smaller than the wavelength [46], such effects can be approximated by using an effective dispersion relation (see Appendix). In practice, the effective value of the surface tension is adjusted according to experimental observations. The derived value, $\gamma_{\text{eff}} = 0.17$ N·m^{-1}, is larger than the usual value for the unperturbed water-air interface, corresponding to an effective increase of the phase velocity inside the artificial crystal. The phenomenological model for the artificial crystal is thus composed of Eq. (5) together with the effective dispersion relation in Eq. (2) and Neumann boundary conditions at the pillars.

We compute phononic band structures $\omega(\mathbf{k})$ along the boundary of the irreducible Brillouin zone (BZ) (namely the path $\Gamma - \mathrm{K} - \mathrm{M} - \Gamma$) as depicted in Fig. 2(a) for the geometry of Fig. 1(b). Phononic band structures are shown for an hexagonal crystal of triangular pillars with lattice constant $a = 8$ mm and $b/a = 0.8$. The phononic band gap extends from 18 to 23 Hz for $\alpha = 30°$, whereas the band gap closes for $\alpha = 0°$. The transmission through a finite crystal sample composed of 5 periods ($\alpha = 30°$) is shown as a function of frequency in Fig. 2(b) for direction ΓK. A good agreement between theory and experiment is observed. At a frequency of 22 Hz, inside the phononic band gap, incident waves are indeed reflected by the crystalline insulator and form a standing wave pattern on the incident side, as illustrated in Fig. 2(c). Full wave numerics are obtained by solving Eq. (5) using the finite element method in Comsol Multiphysics at

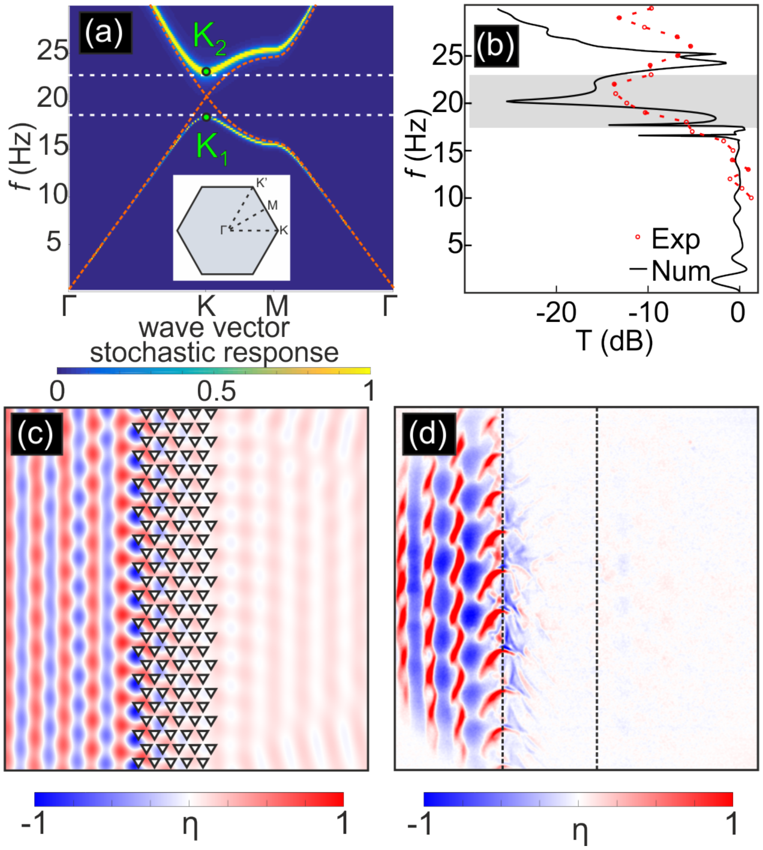

Figure 2. Phononic properties of the water wave crystal of Fig. 1. (a) The dispersion relation is obtained as the response to a stochastic excitation [45] for a water level $h = 7.3$ mm and $\alpha = 30^o$ (the dispersion relation for $\alpha = 0^o$ is the red line). The inset represents the first Brillouin zone (BZ). (b) The measured transmission of a plane wave through a 5 unit cell thick crystal slab (dotted line) is compared with the numerically computed transmission (solid line). (c) Numerical simulation of the reflection of a plane wave at 22 Hz (inside the phononic band gap) on the crystal. (d) Experimentally recorded surface elevation at the same frequency. The boundaries of the crystal are indicated with dashed lines.

a fixed frequency. Fig 2(c) shows an example of the water wave field obtained using this method. PMLs (perfectly matched layers) are used to absorb the outgoing waves.

The experimental setup shown in Fig. 1 is composed of a 24 × 30 cm^2 water wave ripple tank illuminated by stroboscopic light synchronized with a straight paddle, operating at a frequency tunable between 10 and 75 Hz. Shadows caused by light refraction at the sinusoidally modulated water surface are formed onto a screen after reflection off a mirror and are recorded with a camera. A typical experimental wave pattern is shown in Fig. 1(a), without any post-processing. The observed patterns are related to the local surface curvature (a bright fringe indicating a positive curvature and a local elevation of the water level). Hence, after image processing, we obtain a quantity proportional to the vertical elevation of the water surface. Crystal samples are fabricated with 3D additive printing in PLA and a typical sample is shown in Fig. 1(b).

Samples are composed of pillars that are higher than the water level (15 mm, whereas the water level without the crystal equals 7 mm). The experimental transmission for $\alpha = 30°$ is shown as a function of frequency in Fig. 2(b) and is in fair agreement with theory. The experimental image in Fig. 2(d) confirms the strong phononic band gap reflection near 22 Hz.

The 2D hexagonal crystal of rotated opaque triangles supports valley vortex Bloch waves carrying a quantized topological phase [37]. Actually, when $\alpha = 0°$, the plane crystallographic group – or *wallpaper group* – of the crystal is ***p31m***, meaning that there are three 3-fold axes of rotation and three reflection planes, two of which are images in a reflection. When $\alpha \neq 0°$, the symmetry is reduced to that of wallpaper group ***p3***, with only three 3-fold axes of rotation remaining ‡. The Bloch waves defining the phononic band gap follow the same ***p3*** symmetry and show three vortices placed either in between the vertices of the triangles (Bloch waves K_1, with valley topological phase $+\text{sgn}(\alpha)$) or in between the sides of the triangles (Bloch waves K_2, with valley topological phase $-\text{sgn}(\alpha)$) [37]; see Fig. 6 of the Appendix for a representation of the K_1 and K_2 Bloch waves. Note that the vortex centers actually coincide with rotation centers of the crystal.

The crystal B of triangles rotated by $-|\alpha|$ is the image in a *glide reflection* of axis Ox and translation $a/2$ of the crystal A of triangles rotated by $+|\alpha|$. This property can be exploited to construct a domain wall (DW) separating the two non equivalent chiral crystals A and B. As depicted in Fig. 3(a), the DW A-B with A placed above B is different from the DW B-A with B placed above A. Both DWs have the symmetry of the *frieze group* ***p11g***. It was shown for classical non dispersive waves that the DWs support unidirectional edge waves [8]; here we show that the property remains true for dispersive water waves. Both the numerical result in Fig. 3(a) and the corresponding experiment in Fig. 3(b) show that a plane surface wave incident normally from the left is funneled to the right side for the A-B DW, but not for the B-A DW. The reason for this asymmetry is discussed below. The transmission through the topological waveguides was estimated and is presented in Fig. 3(c); again experiment and numerics agree fairly well. Videos of experimental and numerical water wave propagation along the DW are provided in the Supplemental Material.

The edge modes are obtained numerically using the stochastic excitation method, considering a super-cell encompassing 5 rows of each crystals A and B. The phononic band structures for DWs A-B and B-A are shown in Fig. 3(d-e). In each case a edge mode appears inside the phononic band gap, traversing it to connect the systems of bulk bands extending below and above. The A-B edge wave has a negative dispersion – its group velocity is negative for positive wavenumbers, – whereas the B-A edge wave has a positive dispersion. The insets in the figures show the modal distribution of both edge waves. It can actually be verified that the A-B edge wave is composed of K_1 valley vortex waves that are evanescent in the transverse direction. Conversely, the B-A edge

---

‡ For $\alpha = 30°$, the wallpaper group is ***p3m1***, and there are three 3-fold axes of rotation and three reflection planes intersecting at the rotation centers.

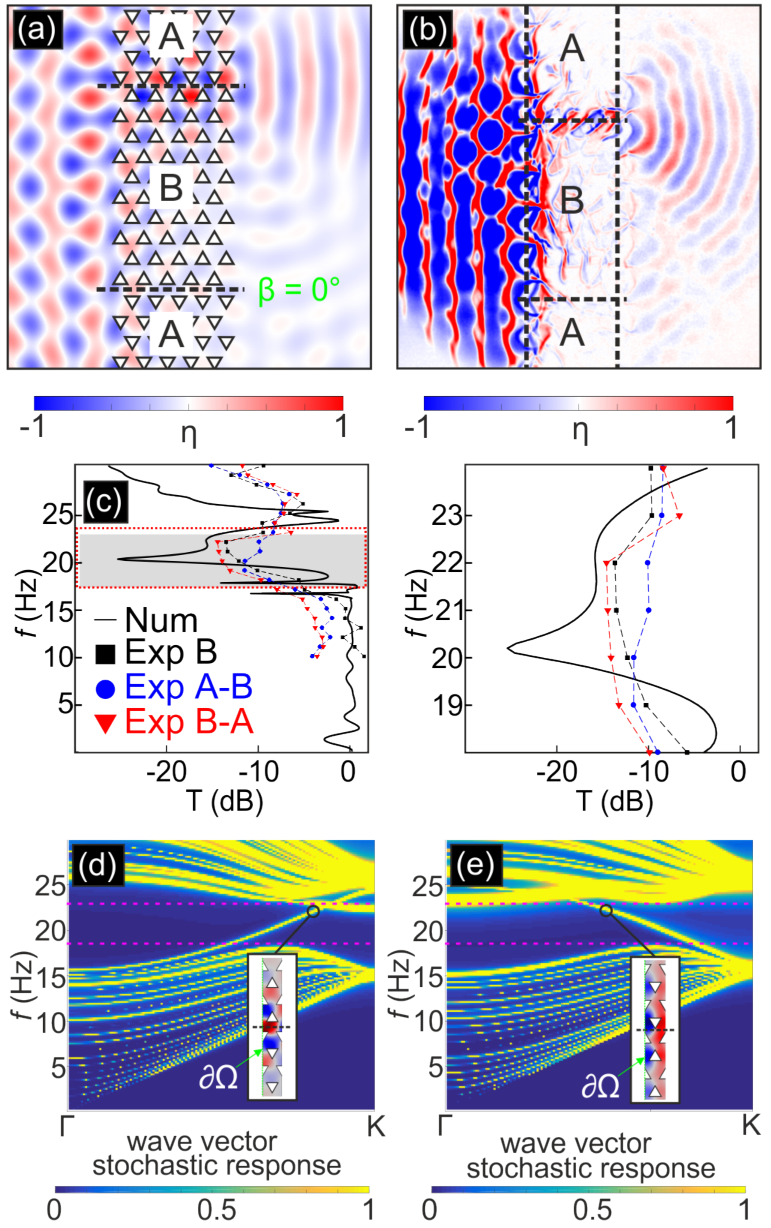

Figure 3. Valley-selective excitation of water wave edge modes for two interfaces at $\beta = 0°$. (a) Numerical simulation and (b) experimental measure of transmission at 22 Hz. (c) Quantitative comparison of the transmission for A-B and B-A interfaces in the experimental and numerical cases (over the full frequency range on the left and zoom on the bandgap region on the right), as well as the case of the domain B. Dots are used for experimentally measured points. Dispersion relations obtained for supercells for the interface B-A in (d) and A-B in (e).

wave is composed of K_2 evanescent valley vortex waves. As further discussed in the Appendix, the sign of the topological charge is in direct connection with the sign of the group velocity of the edge waves.

The possibility of coupling an externally incident plane wave with an edge wave of the domain wall can be evaluated by comparing their modal fields. We evaluate the

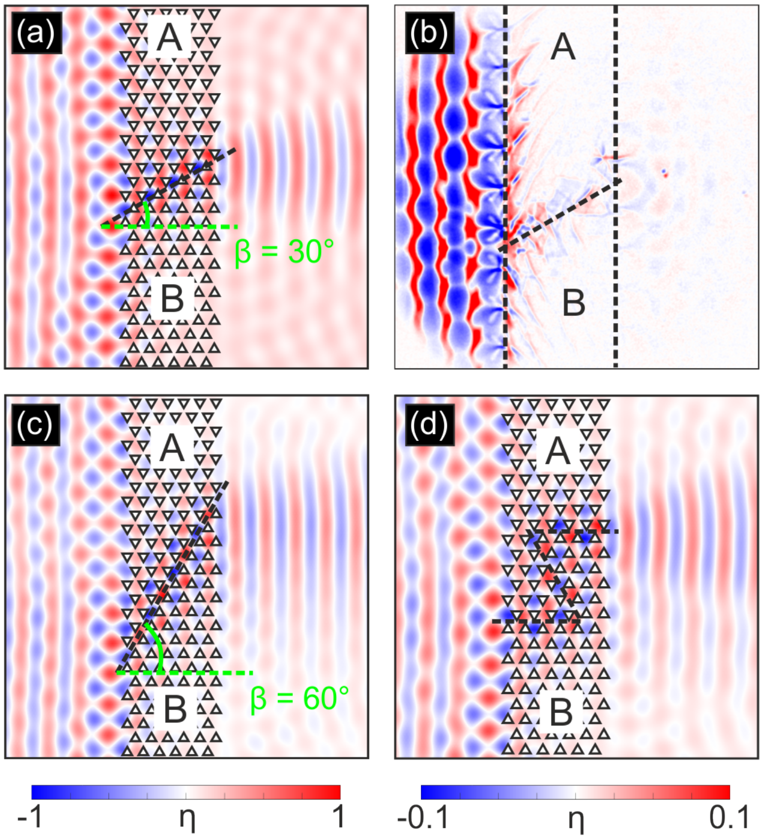

Figure 4. Water wave fields obtained for different geometries of interfaces at 22 Hz. (a) Numerical simulation and (b) experimental transmission of a 30° interface. (c) Numerical simulation of a 60° interface and (d) Numerical simulation of a zigzag shaped interface.

following overlap integral

$$\Psi = \frac{|\int_{\partial\Omega} \eta_0 \cdot \eta(x,y)\ \mathrm{d}y|}{\int_{\partial\Omega} |\eta(x,y)|\ \mathrm{d}y}. \tag{6}$$

computed on the interface $\partial\Omega$ between the crystal and the incidence region. The resulting number, which varies between 0 and 1, measures the matching of the edge mode with a plane wave with amplitude $\eta_0 = 1$ along the interface $\partial\Omega$. We found numerically that $\Psi_{\mathrm{A-B}} \approx 1$ for the A-B DW, and that $\Psi_{\mathrm{B-A}} \approx 0.03$ for the B-A DW. These numbers confirm the asymmetry of coupling of the normally incident plane wave to both edge modes. Furthermore, the overlap integral computed for all Bloch modes (see Appendix) confirms that transmission occurs only along DW A-B for all frequencies.

A DW waveguide making an angle of 30° with respect to the direction of propagation was also fabricated and tested (see Fig. 4(a-b)). Again, theory and experiment agree and show that at the output interface a point-like source emission is obtained. Note that the 30°-rotated DW is not purely of the A-B or B-A type and actually combines K_1 and K_2 vortex states to funnel surface waves. The 60°-rotated DW shown in Fig. 4(c) is of the B-A type. Due to non normal incidence the K_2 vortex edge wave can be excited in this case. Finally, the Z shape DW of Fig. 4(d) combines a series of 120° turns and is of the A-B type. However, the latter crystal has a very low confinement and was thus only tested numerically.

3. Conclusion

To conclude, we performed an experimental demonstration of the existence of topological edge states guided a domain wall of a water wave crystal, in the intermediate regime of gravity-capillary waves. The edge states are a superposition of vortex waves carrying a quantized topological phase [37] and can be described by a classical analogy to the valley Hall effect [8, 47, 7]. A good qualitative agreement between theory and experiments was obtained, with the capillary effects at the interface between water and the crystal modeled via the use of an effective parameter. Our observations extend the reach of topological wave physics to a wide range of physical platforms containing highly dispersive media, not only water wave systems, but also elastic waves and plasmonics.

Acknowledgments

We acknowledge C.-L. Azzopardi, V. Pêcheur, J-F. Manceau, E. Carry, and T. Daugey for samples fabrication, F. Cherioux and S. Benchabane for discussions, and A. Mosset for the measurement setup. This work has been supported by the EIPHI Graduate School (contract ANR-17-EURE-0002) and by the French Investissements d'Avenir program, project ISITE-BFC (contract ANR-15-IDEX-03).

References

[1] Hafezi M 2014 *Phys. Rev. Lett.* **112** 210405
[2] Silveirinha M G 2015 *Phys. Rev. B* **92** 125153
[3] Zhu H, Liu T W and Semperlotti F 2018 *Phys. Rev. B* **97** 174301
[4] Makwana M P and Craster R V 2018 *Phys. Rev. B* **98** 184105
[5] Chen B G g, Upadhyaya N and Vitelli V 2014 *Proc. Nat. Acad. Sci.* **111** 13004
[6] Ma T, Khanikaev A B, Mousavi S H and Shvets G 2015 *Phys. Rev. Lett.* **114** 127401
[7] Vila J, Pal R K and Ruzzene M 2017 *Phys. Rev. B* **96** 134307
[8] Lu J, Qiu C, Ye L, Fan X, Ke M, Zhang F and Liu Z 2017 *Nat. Phys.* **13** 369
[9] Shen Y, Qiu C, Cai X, Ye L, Lu J, Ke M and Liu Z 2019 *Appl. Phys. Lett.* **114** 023501
[10] He C, Ni X, Ge H, Sun X C, Chen Y B, Lu M H, Liu X P and Chen Y F 2016 *Nat. Phys.* **12** 1124
[11] Haldane F D M and Raghu S 2008 *Phys. Rev. Lett.* **100** 013904
[12] Wang Z, Chong Y D, Joannopoulos J D and Soljačić M 2008 *Phys. Rev. Lett.* **100** 013905
[13] Hafezi M, Demler E A, Lukin M D and Taylor J M 2011 *Nat. Phys.* **7** 907
[14] von Klitzing K, Dorda G and Pepper M 1980 *Phys. Rev. Lett.* **45** 494
[15] Thouless D J, Kohmoto M, Nightingale M P and den Nijs M 1982 *Phys. Rev. Lett.* **49** 405
[16] Haldane F D M 1988 *Phys. Rev. Lett.* **61** 2015–2018
[17] Hatsugai Y 1993 *Phys. Rev. Lett.* **71** 3697
[18] Ohgushi K, Murakami S and Nagaosa N 2000 *Phys. Rev. B* **62** R6065
[19] Ren Y, Qiao Z and Niu Q 2016 *Rep. Prog. Phys.* **79** 066501
[20] Kane C L and Mele E J 2005 *Phys. Rev. Lett.* **95** 146802
[21] Kane C L and Mele E J 2005 *Phys. Rev. Lett.* **95** 226801

[22] Andrei B B and Shou-Cheng Z 2006 *Phys. Rev. Lett.* **96** 106802

[23] Bernevig B A, Hughes T L and Zhang S C 2006 *Science* **314** 1757

[24] Khanikaev A B, Hossein M S, Tse W K, Kargarian M, MacDonald A H and Shvets G 2012 *Nat. Mater.* **12** 223

[25] Hafezi M, Mittal S, Fan J, Migdall A and Taylor J M 2013 *Nat. Photon.* **7** 1001

[26] Lu L, Joannopoulos J D and Soljačić M 2014 *Nat. Photon.* **8** 821

[27] Peng Y G, Qin C Z, Zhao D G, Ya-Xi S, Xu X Y, Bao M, Jia H and Zhu X F 2016 *Nat. Commun.* **7** 13368

[28] Khanikaev A B, Fleury R, Mousavi S H and Alu A 2015 *Nat. Commun.* **6** 8260

[29] Yang Z, Gao F, Shi X, Lin X, Gao Z, Chong Y and Zhang B 2015 *Phys. Rev. Lett.* **114** 114301

[30] Gao F, Gao Z, Shi X, Yang Z, Lin X, Xu H, Joannopoulos J D, Soljačić M, Chen H, Lu L, Chong Y and Zhang B 2016 *Nat. Commun.* **7** 11619

[31] Nash L M, Kleckner D, Read A, Vitelli V, Turner A M and Irvine W T M 2015 *Proc. Nat. Acad. Sci.* **112** 14495

[32] Süsstrunk R and Huber S D 2015 *Science* **349** 47

[33] Süsstrunk R and Huber S D 2016 *Proc. Nat. Acad. Sci.* **113** E4767–E4775

[34] Huber S D 2017 *Nat. Phys.* **12** 621

[35] Raghu S and Haldane F D M 2008 *Phys. Rev. A* **78** 033834

[36] Hsieh D, Qian D, Wray L, Xia Y, Hor Y S, Cava R J and Hasan M Z 2008 *Nature* **452** 970

[37] Lu J, Qiu C, Ke M and Liu Z 2016 *Phys. Rev. Lett.* **116** 093901

[38] Qian K, Apigo D J, Prodan C, Barlas Y and Prodan E 2018 *Phys. Rev. B* **98** 155138

[39] Zhang Z, Tian Y, Wang Y, Gao S, Cheng Y, Liu X and Christensen J 2018 *Advanced Materials* **30** 1803229

[40] Zhang X, Xiao M, Cheng Y, Lu M H and Christensen J 2018 *Communications Physics* **1** 97

[41] Miles J W 1978 *Journal of Fluid Mechanics* **88** 793

[42] Hu X, Shen Y, Liu X, Fu R, Zi J, Jiang X and Feng S 2003 *Phys. Rev. E* **68** 037301

[43] Hu X, Shen Y, Liu X, Fu R and Zi J 2004 *Phys. Rev. E* **69** 030201

[44] Jeong T S, Kim J E, Park H Y and Lee I W 2004 *Appl. Phys. Lett.* **85** 1645

[45] Laude V and Korotyaeva M E 2018 *Phys. Rev. B* **97** 224110

[46] Dupont G, Kimmoun O, Molin B, Guenneau S and Enoch S 2015 *Phys. Rev. E* **91** 023010

[47] Pal R K and Ruzzene M 2017 *New Journal of Physics* **19** 025001

[48] Llowarch W 1956 *Nature* **178** 587

[49] Hajnal J, Templer R and Upstill C 1984 *European Journal of Physics* **5** 81

[50] Ströbel B 2011 *American Journal of Physics* **79** 581–590

Appendix

We describe in more detail experimental methods, the effective dispersion relation, the phononic band structures, the overlap integral, and the vortex Bloch waves of the water wave crystals considered in this work.

Experimental methods

The experimental apparatus we use to observe and image water waves is shown in Figure 1. Light impinging from a frequency modulated source is steered at the interface between water and air, travels through the thin water tank and reaches the observation screen after reflection off a mirror. A common phenomenological interpretation of the bright lines observed on the screen is to link them to the wave crests that act as cylindrical collecting lenses, while shades are linked with wave troughs that behave as diverging lenses. However, the situation is in general far more complex and the relationship between the pattern of light and shade on the screen and the ripple elevation above the average water surface level is not straightforward [48]. In fact, it should be described as the intersection of a three-dimensional caustics with the projection plane, taking into account blurring due to source extension and chromatic dispersion [49]. Still, this statement is mostly true for waves with strongly curved interfaces, that is for short wavelength and large amplitude [50], and for cases where we observe interaction of multiple waves [49]. In our case, with mostly very low wave amplitude in the crystal and beyond, the light and shade patterns are not significantly affected by these limitations and bear direct link with the surface curvature, allowing to easily extract the significant quantities of the ripples using image processing.

Effective dispersion relation

We consider waves propagating in linear, irrotational, and inviscid water. The velocity vector derives from a velocity potential as $\mathbf{v} = \nabla\Phi$. For the geometry depicted in Figure 1 we can apply the method of separation of variables to write [42]

$$\Phi(x, y, z, t) = \mathrm{Re}[\phi(x, y)\cosh(\kappa(z + h))e^{-\imath\omega t}], \tag{7}$$

with the water-air interface at $z = 0$. With this device, the original three-dimensional problem is cast into a two-dimensional partial differential equation (1) with Neumann boundary condition at the pillar-water interface.

Without the pillar in the hexagonal unit cell, periodicity is artificial and plane wave propagation is governed by the dispersion relation (2) with surface tension $\gamma = 0.073$ N·m^{-1} accounting for the water-air interface. The dispersion relation is plotted in Fig. 5(b) and can be rewritten

$$\frac{1}{2}\rho\omega^2 = \frac{1}{2}(\rho g\kappa + \gamma\kappa^3)\tanh(\kappa h), \tag{8}$$

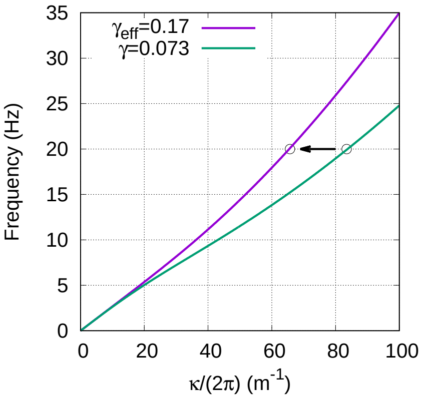

Figure 5. Dispersion relation for water waves for a water level $h = 7.3$ mm.

with $\rho = 1000$ kg·m^{-3} and $g = 9.81$ m·s^{-1}. Under that form, the left-hand side accounting for the kinetic energy density density is balanced by the right-hand side accounting for the potential energy density. The potential energy has two contributions, from gravity and from surface tension.

With the pillar in place, there is an additional surface contribution to the potential energy at the pillar-water interface. We do not attempt to model that contribution precisely, but assume that it has a form similar to the term for the water-air interface, and we remark that a positive surface tension must lead to an increase in the total potential energy for one unit cell of the crystal. Since the kinetic energy must match that increase for any solution of the Helmholtz equation, the phase velocity ω/κ must increase accordingly. The increase in phase velocity is determined experimentally by comparing the change in wavelength when the crystal is not in place and when it is. Considering the crystal without a band gap ($\alpha = 0°$) and measuring the wavelength at a frequency of 20 Hz, we monitor the change in wavenumber in Fig. 5. We infer the effective value $\gamma_{\text{eff}} = 0.17$ N·m^{-1} for our samples. Of course, that particular value depends on the crystal details, especially on the filling fraction, and should not be given a microscopic meaning. It is an effective parameter in the metamaterial sense, inferred for the unit cell of the crystal considered as a whole. As a result, Eqs. (2) and (5) of the main manuscript form a phenomenological model of the water wave crystal, sufficient for qualitative comparison with experiment. It remains that obtaining a more precise three-dimensional model would be necessary for a quantitative analysis.

Phononic crystal for water waves

The stochastic excitation method [45] is used to obtain the phononic band structure via finite element implementation of equation (5) in the main manuscript. This equation is for a scalar unknown field, the elevation $\eta(x, y)$, and has the form of a dispersive Helmholtz equation. The main difficulty is that the coefficients of the equation depend on frequency. The stochastic excitation method circumvents the difficulty by fixing

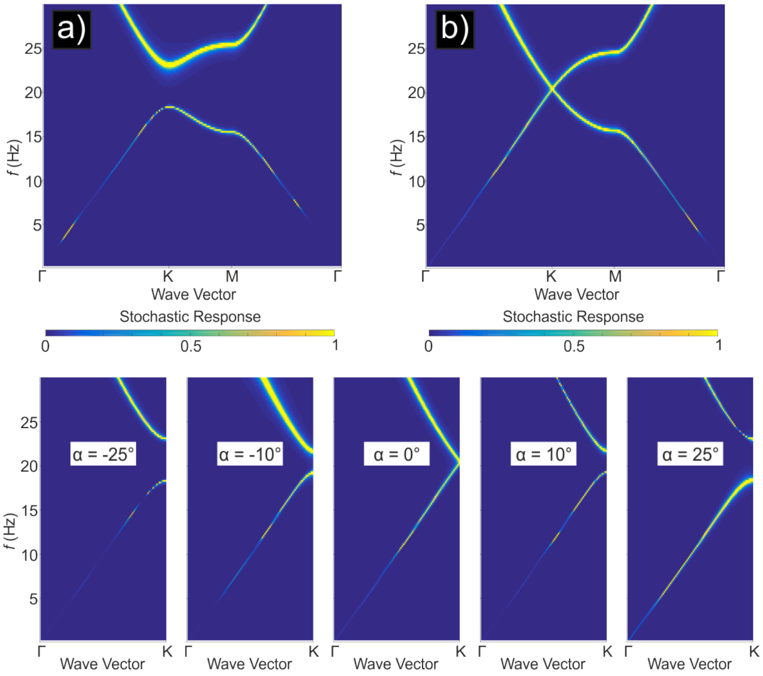

Figure 6. Computed dispersion relations obtained as the response to a stochastic excitation [45] for a water level $h = 7.3$ mm for $\alpha = 30^o$ in (a), $\alpha = 0^o$ in (b). In the lower row of panels, 5 different angles are used and only the Brillouin zone direction of interest, i.e. ΓK is depicted.

both frequency ω and wavenumber k and by observing the response of the system to a spatially random force distributed inside the unit-cell. The unit-cell is the elementary hexagon depicted in Fig. 1(b) of the main manuscript; dimensions are given in the caption of the latter figure.

The phononic band structures plotted in Fig. 6 show that the phononic band gap is initially closed when the angle of rotation of the triangular pillars is zero, $\alpha = 0°$. When α is increased or decreased, the phononic band appears symmetrically and gradually opens until its maximum value obtained for $|\alpha| = 30°$ (see the lower row of the figure).

Vortex Bloch waves

Decisive information is obtained regarding the topological properties of the crystal by observing the Bloch waves belonging to the two bands defining the phononic band gap. The space group symmetry of the crystal is illustrated in Fig. 7 for different values of the angle of rotation α. The wallpaper group changes from ***p31m*** for $\alpha = 0°$ to ***p3*** for $0° < |\alpha| < 30°$, and to ***p3m1*** for $|\alpha| = 30°$. Following Ref. [37], we display in Fig. 8 the Bloch waves K_1 and K_2 lying on the first and the second band at the K point of the first Brillouin zone for $\alpha = 30°$.

Bloch wave K_1 follows the ***p3*** symmetry. It mainly features three vortices centered in the region where vertices of the triangles are closest. Note that the direction of rotation of the vortices is opposite when the sign of α is reversed. They turn toward

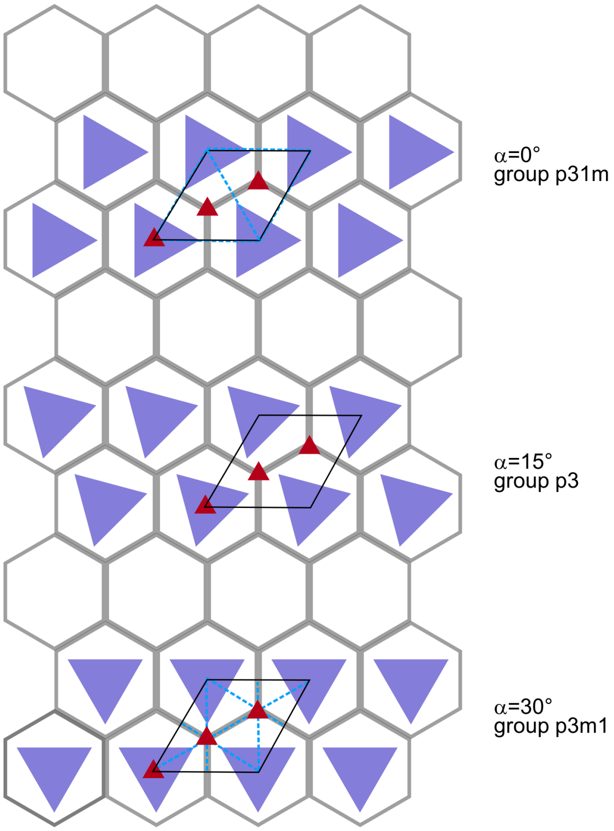

Figure 7. Wallpaper groups for crystals with different values of rotation angle α. 3-fold rotation centers are indicated with red triangles; reflection axes are indicated with dotted lines.

the left for positive α and toward the right for negative α. Bloch waves K_1 for $\pm\alpha$ are images in a glide reflection of axis Ox and translation by half the lattice constant (they are also images in glide reflections rotated by $2\pi/3$ and $4\pi/3$).

Bloch wave K_2 also follows the ***p3*** symmetry and features three vortices centered in the region where sides of the triangles are farther away. The direction of rotation of the vortices is opposite when the sign of angle α is reversed, and is the opposite of the direction of rotation of K_1 vortices. As in the case of K_1 Bloch waves, Bloch waves K_2 for $\pm\alpha$ are images in a glide reflection of axis Ox and translation by half the lattice constant (they are also images in glide reflections rotated by $2\pi/3$ and $4\pi/3$).

Vortex edge waves propagating along a domain wall

Bloch edge waves are obtained by considering a supercell of type A-B (A above B) or B-A (B above A), as explained in the main text. The interest is mainly for their field distribution for frequencies belonging to the phononic band gap. In this case, since the band gap is complete, they must be evanescent in the transverse direction, i.e. their amplitude decays exponentially away from the domain wall (DW). This is confirmed by the modal shapes shown in Fig. 9.

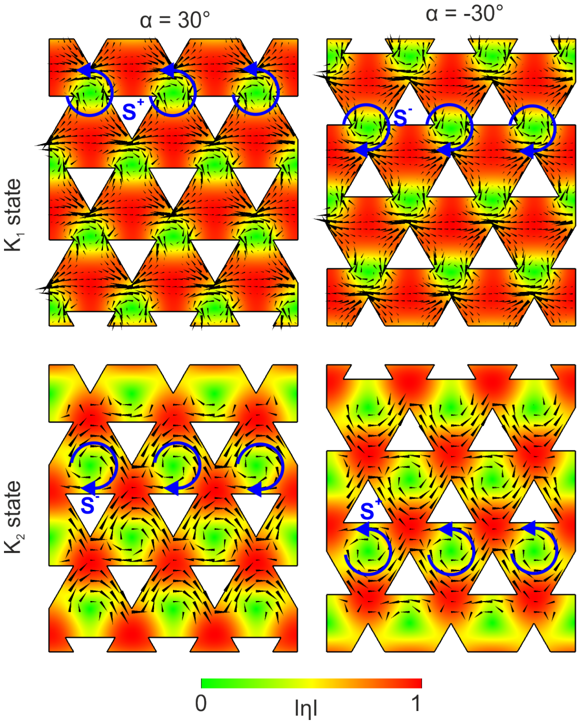

Figure 8. Vortex Bloch waves at the K point of the first Brillouin zone. The color scale is for the modulus of water elevation (normalized). The distribution of the Poynting vector is shown with arrows. Vortex Bloch waves K_1 and K_2 are shown for pillars rotated by either $\alpha = 30°$ or $\alpha = -30°$.

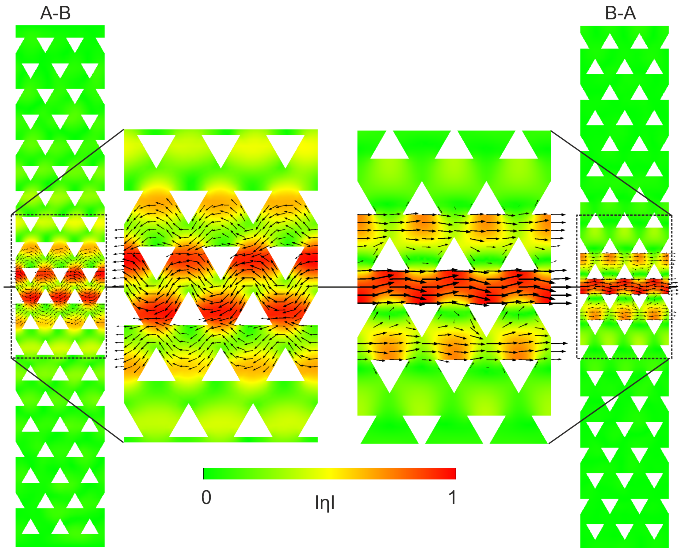

Figure 9. Domain wall vortex edge waves. The color scale is for the modulus of water elevation (normalized). The distribution of the Poynting vector is shown with arrows. The A-B domain wall is shown on the left and the B-A domain wall is shown on the right. Close-up views are provided in order to illustrate the distribution of the Poynting vector.

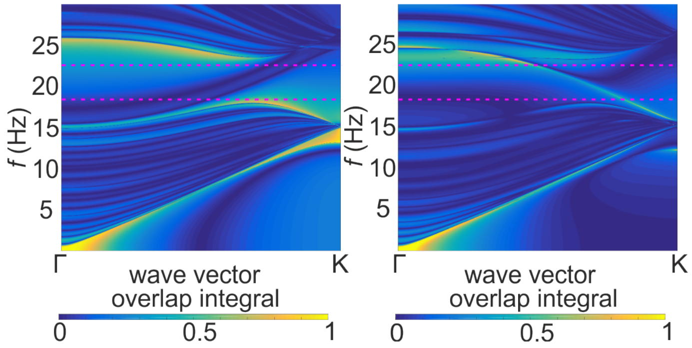

Figure 10. Overlap integral for the B-A domain wall (left) and the A-B domain wall (right) versus wavenumber (horizontal axis) and frequency (vertical axis).

The vortex Bloch waves K_1 and K_2 of Fig. 8 sit at the edges of the phononic band gap and are thus not evanescent. Because the eigenvalue problem is analytic in the complex plane as a function of the wavenumber k, we infer that the evanescent Bloch waves inside the band gap can be continuously deformed from the K_1 and K_2 Bloch waves. Since the edge waves are necessarily composed of such evanescent Bloch waves of the crystal, matched at the DW, the formation of the edge waves can be understood as a superposition of vortex Bloch waves. From the field distributions in Fig. 9, we infer that the edge mode of the A-B DW is composed of K_1 evanescent Bloch waves and that the edge mode of the B-A DW is composed of K_2 evanescent Bloch waves. The Poynting vector arrows further confirm that the A-B DW mode propagates with opposite phase and group velocities, while the B-A DW mode propagates with phase and group velocities of the same sign.

Overlap integral

The overlap integral measuring the coupling with a normally incident plane wave can be computed for all Bloch waves of the DW supercells, similarly to the phononic band structures shown in Fig. 3(d-e). The result is shown in Fig. 10 for domain walls A-B and B-A. It can be clearly observed that the B-A DW mode cannot be exited by a plane wave. This can be intuitively understood from the odd and even nature of the A-B and B-A edge modes, shown in Fig. 9.